POLITECNICO DI TORINO
Repository ISTITUZIONALE

Effects of phase scintillation on the GNSS positioning error during the September 2017 storm at Svalbard

Original
Effects of phase scintillation on the GNSS positioning error during the September 2017 storm at Svalbard / Linty, N.U., Minetto, A., Dovis, F., Spogli, L.. - In: SPACE WEATHER. - ISSN 1542-7390. - ELETTRONICO. - 16:9(2018), pp. 1317-1329. [10.1029/2018SW001940]

Availability:
This version is available at: 11583/2712644 since: 2018-11-14T16:41:45Z

Publisher:
Wiley

Published
DOI:10.1029/2018SW001940

Terms of use:

This article is made available under terms and conditions as specified in the corresponding bibliographic description in the repository

Publisher copyright

(Article begins on next page)

18 November 2026

Space Weather

RESEARCH ARTICLE
10.1029/2018SW001940

Special Section:
Space Weather Events of 4-10 September 2017

Effects of Phase Scintillation on the GNSS Positioning Error During the September 2017 Storm at Svalbard

Nicola Linty[1], Alex Minetto[1], Fabio Dovis[1], and Luca Spogli[2,3]

[1]Department of Electronics and Telecommunications, Politecnico di Torino, Turin, Italy, [2]Istituto Nazionale di Geofisica e Vulcanologia, Rome, Italy, [3]SpacEarth Technology, Rome, Italy

Abstract In early September 2017, several space weather events triggered disturbed conditions of the near-Earth space. The combination of two coronal mass ejection arrivals, associated with an X-class flare, caused a strong geomagnetic storm on 7 and 8 September, thus inducing diffuse ionospheric phase scintillations on Global Navigation Satellite System (GNSS) signals. This work analyzes the effects and the actual impact of such phase scintillations on transionospheric Global Positioning System (GPS) signals and on related positioning accuracy. The research focuses in particular on high-latitude GPS L1 data, recorded during a test campaign in Svalbard, Norway. The joint effect of satellites at low elevation and the exposure of ionosphere to the geospace forcing make navigation a critical task for such a challenging environment. Data analysis shows that the performance of carrier smoothing algorithms was affected by the presence of moderate and strong phase scintillation. It is shown in this study that positioning errors double when GPS signals affected by scintillation are used. This work shows that scintillations induce a considerable clustering effect on the smoothed positioning solutions; therefore, a methodology to automatically and autonomously detect the boundaries of the scintillation event is suggested according to such an high-level effect. The use of software-defined radio receivers for automatically capturing and processing GNSS data affected by scintillation is an added value to the analysis, as it offers the possibility to implement advanced signal processing techniques and a deeper observation of the impact of scintillations on the signals.

Plain Language Summary Global Navigation Satellite Systems, such as GPS, are widely used for positioning, navigation, and scientific purposes. However, such signals are subject to severe nuisances as they cross the upper part of the Earth atmosphere, the ionosphere. In particular, space weather events, as the one occurred in early September 2017, can further disrupt the quality of the received signals and, in turn, the accuracy, availability, continuity, and reliability of the positioning solution. In this work we show how the September 2017 storm affected GPS signals, focusing on data captured at Svalbard Islands, a region highly disturbed by space weather events, due to its proximity to the geomagnetic pole. More in detail, we focus on the actual impact of ionospheric phase scintillation induced by the storm. Data analysis shows that the performance of certain algorithms, employing phase measurements to increase the positioning accuracy, such as carrier smoothing, is affected by the presence of moderate and strong phase scintillation. The positioning error doubles, when compared to the case in which no scintillation is present. The work also shows that scintillation induces a considerable clustering effect on the positioning solutions, thus suggesting a novel methodology for automatically and autonomously detecting space weather events.

Key Points:
- GPS L1 signals affected by scintillation were automatically recorded during the September 2017 geomagnetic storm
- Carrier smoothed positioning error was analyzed in the presence of phase scintillation
- Clustering of GPS positioning solutions was investigated for the detection of scintillation events

Correspondence to:
N. Linty,
nicola.linty@polito.it

Citation:
Linty, N., Minetto, A., Dovis, F., & Spogli, L. (2018). Effects of phase scintillation on the GNSS positioning error during the September 2017 storm at Svalbard. *Space Weather*, *16*. https://doi.org/10.1029/2018SW001940

Received 1 MAY 2018
Accepted 14 AUG 2018
Accepted article online 23 AUG 2018

©2018. The Authors.
This is an open access article under the terms of the Creative Commons Attribution-NonCommercial-NoDerivs License, which permits use and distribution in any medium, provided the original work is properly cited, the use is non-commercial and no modifications or adaptations are made.

1. Introduction

Geomagnetic and ionospheric storms severely affect the quality of transionospheric electromagnetic radio signals (Van-Dierendonck et al., 1993; Wernik et al., 2004). Among which, Global Navigation Satellite System (GNSS) signals, broadcast by medium Earth orbit satellites in the L-band (1–2 GHz), are considered in this study. Their propagation through the ionosphere is characterized by refraction, due to the dispersive nature of the ionosphere. In addition, under disturbed conditions, electron density irregularities cause diffraction and scattering of GNSS signals, known as ionospheric scintillations (Alfonsi et al., 2011; Doherty et al., 2003). The received GNSS signals may then experience deep amplitude fading (amplitude scintillations) and random fluctuations on the carrier phase (phase scintillations; Dubey et al., 2006). At high latitude, such fluctuations are due to the presence of fast-moving ionospheric irregularities making the ionospheric environment extremely dynamical and complex (Basu et al., 2002; De Franceschi et al., 2008). Such irregularities may originate from

patches of plasma density or troughs, which can host the formation of smaller-scale density structures (from hundreds of kilometers down to centimeter scale) in correspondence with their boundaries (Spogli et al., 2013). The scale of the irregularities determines the amplitude and phase response of the transionospheric electromagnetic wave: The Fresnel filtering mechanism strongly suppresses the amplitude contribution for scales larger than the Fresnel scale (Alfonsi et al., 2011). In the case of L-band, the Fresnel scale is of the order of hundreds of meters. Moreover, the phase scintillation directly reflects the plasma dynamics and it is likely linked with an increased probability of signal loss of lock (Forte, 2007).

On one hand, ionospheric scintillations may severely damage the quality of received GNSS signals and, in turn, the accuracy and reliability of the Position, Velocity and Time (PVT) solution. Therefore, the ionosphere is the highest source of errors in single frequency GNSS receivers, if not properly compensated (Jiao et al., 2013).

On the other hand, GNSS signals and GNSS receivers can be used as a complementary tool to monitor the ionospheric behavior. Networks of receivers allow a simultaneous, continuous, dense, and cheap monitoring of the phenomenon through many pierce points.

Remote sensing of the ionosphere can be carried out by inverting the traditional positioning equation, exploiting the known information about the receiver location and time (Curran et al., 2014). A direct investigation of the phenomenon can be performed through the evaluation of specific scintillation indexes (Van-Dierendonck et al., 1993). The σ_ϕ index is a measure of phase scintillations: It corresponds to the standard deviation of the detrended carrier phase measurement. The σ_ϕ, along with the amplitude index *S*4, is widely used to assess the impact of scintillation on the signal. Scintillation is declared present if σ_ϕ exceeds a predefined thresholds, typically set to 0.25 rad (Dubey et al., 2006). Scintillation indexes are provided by professional Ionospheric Scintillation Monitoring Receivers (ISMRs); alternatively, customized software-defined radio (SDR) GNSS data grabbers and fully software receivers can be used (Cristodaro et al., 2018; Linty et al., 2015). In this study an SDR-based GNSS receiver is used to process the signals to compute the positioning solution and to estimate the phase index exploited for the scintillation analysis.

1.1. Rationale of the Work

Several works in the last decades have been focused on the degradation of GNSS receivers' performance due to ionospheric impairments (Groves et al., 2000; Jiao et al., 2013). Scintillation indexes behavior and direct effects on tracking loops have been deeply investigated in literature (Groves et al., 2000). More recently, researchers have discussed carrier phase positioning and related effects when phase measurements are corrupted by unwanted phenomena (Myer & Morton, 2018). Differently, this work is focused on the main output of the navigation algorithm: the estimated position of the user.

Traditional code-based PVT solution is characterized by values of uncertainty, which are generally too large to observe the minor effects due to scintillation. Differently, positioning techniques involving carrier phase measurements, such as carrier smoothing, allow one to reach higher levels of precision. However, they are prone to biases and errors due to nuisances affecting the signal phase; for example ionospheric scintillations. Preliminary analysis of the smoothed positioning solutions showed unexpected clusterization phenomena. In this study, a deeper investigation outlined that this effect can be attributed to scintillation events rather than to other sources of errors. On one hand, it facilitates the statistical analysis of ionospheric events and of their impact on positioning solutions. On the other hand, it offers a novel approach for events detection, with a limited computational effort and directly related to the positioning solutions rather than to the quality of the received signal. Furthermore, the effect can be magnified by properly tuning the smoothing algorithm.

1.2. The Geomagnetic Storm of 6–10 September 2017

The extreme solar activity at minimum of solar cycle 24, which occurred between 4 and 10 September 2017, was one of the hardest in almost a decade after more than a year without noticeable events (Schwadron et al., 2018). The stormy conditions have been driven by the Active Region AR2673, from which four X-class eruptions have emerged, including the strongest flare (class X9.3) of the current solar cycle, occurred on 6 September (Tassev et al., 2017). Such a flare triggered also a geoeffective coronal mass ejection (CME) event, which triggered disturbed magnetospheric and ionospheric conditions (Vanlommel & Van der Linden, 2017).

To provide a quantitative overview of the phenomena, time profiles of AU (blue) and AL (red) auroral indexes (panel a), of AE (red) and AO (green) auroral indexes (panel b), of the disturbance storm time (DST; panel c), and *Kp* (panel d) indexes of geomagnetic disturbance are reported in Figure 1. By looking at DST index (panel c),

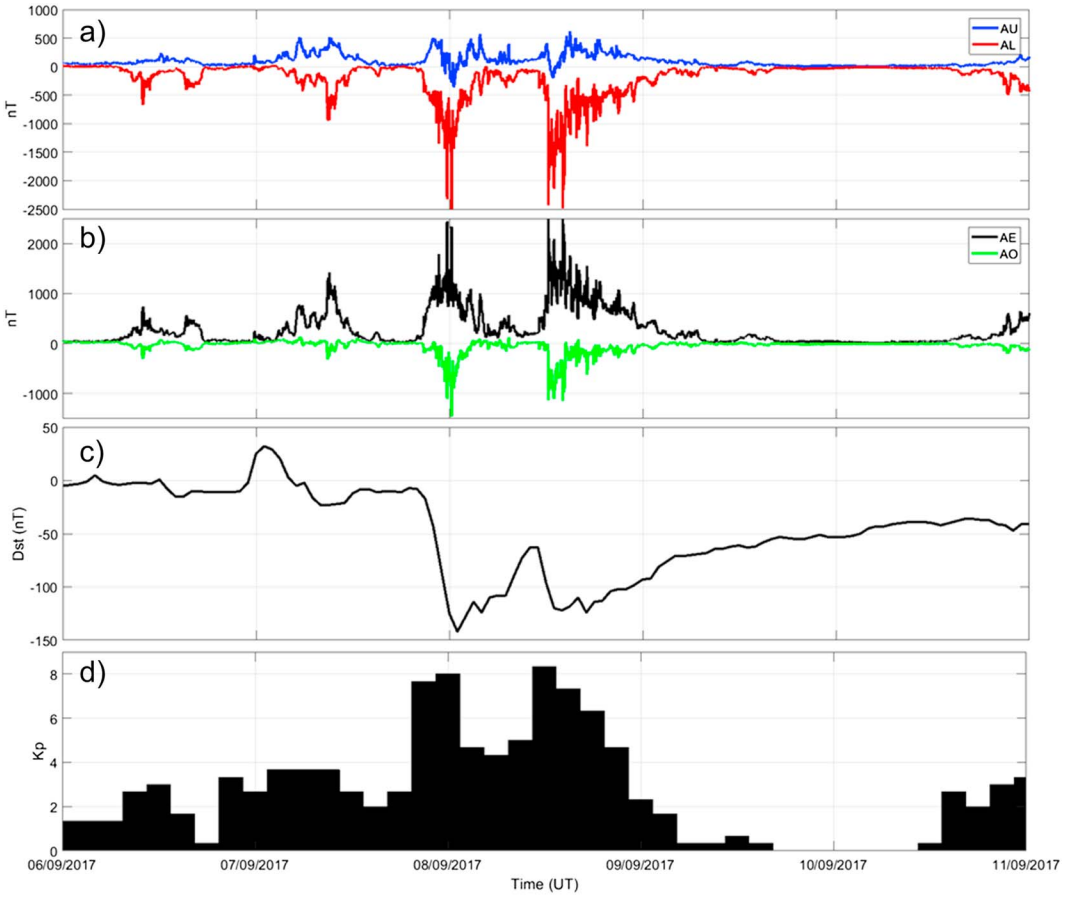


Figure 1. Time profiles of (a) AU (blue) and AL (red) auroral indexes, (b) of AE (red) and AO (green) auroral indexes, of (c) DST, and (d) *Kp* indexes of geomagnetic disturbance in September 2017.

the sudden storm commencement (SSC) of the geomagnetic storm was on early 7 September, while the peak was on early 8 September (DST = −142 nT), with signatures of substorm activity during the beginning of the recovery phase (again on 8 September). At the peak of the storm, the value of *Kp* was 8, reaching 8+ later in the day, making the storm a G4-class storm, that is, a severe geomagnetic storm according to the National Oceanic and Atmospheric Administration G-scale. The storm also triggered strong auroral activity, as visible from the time profiles of the auroral indexes (Figures 1a and 1b). In particular, a strong intensification of both the eastward and westward auroral electrojects is found in correspondence to the SSC, peak and substorm main signature of the storm.

1.3. Paper Outline

A brief description of scintillation effects on GNSSs and on the geomagnetic storm of September 2017 is provided in this introduction. Section 2 details the methodology used in this work, concerning the analysis of the GNSS positioning error and of carrier smoothing algorithms. The third section describes the measurement campaign carried out in Longyearbyen (Svalbard, Norway) and the paradigm of SDR technology for GNSS receivers. Results, in terms of scintillation indexes linear plots analysis, positioning errors, and clustering effects on the positioning solutions, induced by phase scintillations, are reported in section 4. Finally, the conclusions of the work are drawn, along with directions for further research on the topic.

2. Methodology

Some major theoretical aspects of GNSS positioning are recalled in this section. Fundamentals on positioning error are discussed to provide the theoretical background for a rigorous investigation of scintillation impacts. Carrier smoothing positioning is also introduced by focusing on its potential vulnerabilities.

2.1. GNSS Positioning Error

In the domain of GNSS, the positioning error is modeled by means of two contributions: the geometrical dilution of precision (GDOP) and the user equivalent range error (UERE; Misra & Enge, 2006). The GDOP is computed from the observation matrix **G**:

$$\mathbf{G} = \begin{pmatrix} a_{1,x} & a_{1,y} & a_{1,z} & 1 \\ a_{2,x} & a_{2,y} & a_{2,z} & 1 \\ \vdots & \vdots & \vdots & 1 \\ a_{N,z} & a_{N,y} & a_{N,z} & 1 \end{pmatrix}, \tag{1}$$

where the first three coefficients of each row are the Earth Centered Earth Fixed (ECEF) components of a unitary vector directed toward the n-th satellite, while N is the number of satellites available for the PVT. **G** describes the geometry of the observed constellation thus having a direct impact on the estimated solution. Each Cartesian component of the estimated position vector $\hat{\mathbf{x}} = \left[\hat{x}, \hat{y}, \hat{z}\right]$ is characterized by its own standard deviation, but GDOP is typically considered for the evaluation of the overall impact as follows:

$$\text{GDOP} = \sqrt{\text{Tr}(\mathbf{G}^T\mathbf{G})^{-1}}, \tag{2}$$

where Tr(·) is the *trace* operand and is defined as the sum of the elements of the diagonal of a square matrix.

Ideally, satellite-to-receiver range measurements correspond to geometrical Euclidean distances between the respective positions. Actually, they are related to the measurement of the signal time of flight thus resulting in alteration by unwanted delays and asynchronous clocks between transmitters and receivers (Bradford et al., 1996). These impairments have to be compensated in order to perform reliable positioning and navigation with acceptable performance. The actual measured distance varies due to a set of error terms, among which scintillations play a relevant role, thus being unpredictable and difficult to model.

The UERE is the residual error on the range measurements between satellites and receivers, assuming all the biases are properly corrected (Misra & Enge, 2006). It is assumed to be zero mean Gaussian distributed with variance, σ^2_{UERE}:

$$UERE \sim \mathcal{N}(0, \sigma^2_{\text{UERE}}). \tag{3}$$

In static scenario, least mean square (LMS) algorithm is adopted to solve for the trilateration problem from known satellites positions and the aforementioned set of range measurements. In a static scenario, the realizations of the ECEF coordinates vector, $\hat{\mathbf{x}}$, are obtained as output of the positioning algorithm.

Given the estimated position vector $\hat{\mathbf{x}}$ at a given time instant t, the associated error covariance matrix is defined as follows:

$$\mathbf{P}_{\mathbf{x}}(t) = \sigma^2_{\text{UERE}}\,(\mathbf{G}^T\mathbf{G}). \tag{4}$$

The standard deviation of the positioning error is hence obtained from the following:

$$\sigma_\epsilon = \sigma_{\text{UERE}} \cdot \sqrt{\text{Tr}(P_{\mathbf{x}})} = \sigma_{\text{UERE}} \cdot \text{GDOP}. \tag{5}$$

The impact of ionospheric disturbances is expected to alter the behavior of the positioning error along the time. Therefore, this study is addressed toward a better understanding of their consequences on the covariance and bias of such a metric.

2.2. Carrier Smoothing Algorithms

The main difference between mass-market cheap receivers and professional expensive receivers is the kind of range measurement used for the computation of the PVT solution. While mass-market single frequency receivers exploit *code pseudoranges*, computed starting from the estimation of the signal code delay, professional multifrequency receivers make use of carrier phase measurements. Code measurements are unambiguous but noisy; on the contrary, carrier phase measurements are much more precise but inherently ambiguous, and the process to solve for the integer ambiguity is not affordable by mass-market receivers (Misra & Enge, 2006).

An intermediate solution is based on the combination of code and carrier phase measurements through a process denoted as carrier smoothing filtering (Petovello et al., 2015). Let $\rho(t)$ and $\Theta(t)$ be the code and carrier

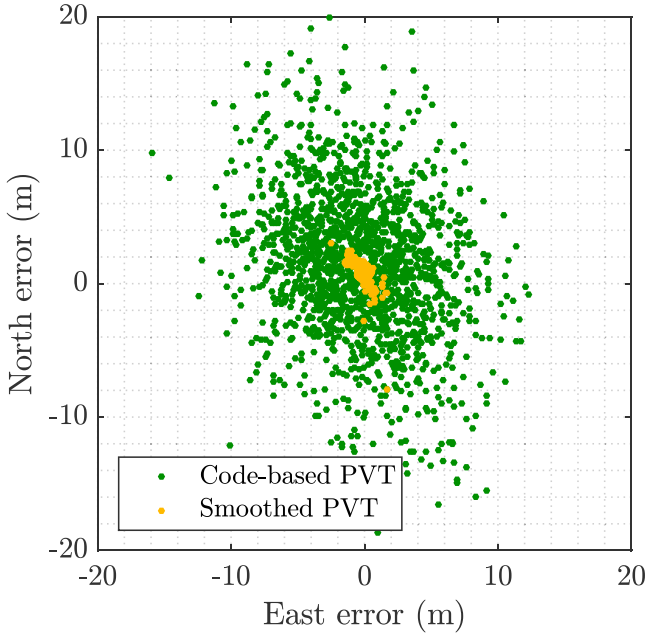


Figure 2. Positioning error in E-N coordinates for code-based and smoothed algorithms ($W = 100$). PVT = Position, Velocity and Time.

pseudorange, respectively. The smoothed pseudorange, at epoch t_n, can then be defined by the following finite difference equation:

$$\bar{\rho}(t_n) = \frac{1}{W}\rho(t_n) + \frac{W-1}{W}\left[\bar{\rho}(t_{n-1}) + \Theta(t_n) - \Theta(t_{n-1})\right], \quad (6)$$

where W is a weight coefficient and $\Theta(t_n) - \Theta(t_{n-1})$ is called *delta pseudorange* and is obtained by differencing subsequent epochs. As long as no carrier cycle slips occur, the integer ambiguity term is constant and disappears thanks to the difference operation. While the noise term of the code measurement $\rho(t_n)$ is at meter level, the noise term of the carrier phase measurement $\Theta(t_n)$ is at centimeter level. Furthermore, if the two measurement epochs are close enough to each other, in the order of a few seconds, the ionospheric delay term can be considered constant and thus disappears in the delta pseudorange. The parameter W controls the weight of the code and carrier contributions. A higher W assures a lower noise variance but introduces a bias in the smoothed code pseudorange, due to the different sign of the ionospheric delay in code and phase measurements, denoted as code-carrier divergence. Carrier smoothing is indeed a valuable technique to improve the accuracy of the positioning solution in mass-market single frequency receivers, which cannot exploit double frequency measurements for compensating the ionospheric delay and cannot employ pure carrier phase measurements.

Figure 2 shows an example of positioning solution, over 30 min of data. The error with respect to the true position, in east-north coordinates, is plotted. The positioning obtained by exploiting code-based measurements is compared to the solution obtained exploiting carrier smoothing. The smoothing weight W was set to 100. The accuracy of the results improves by about 1 order of magnitude when smoothing is enabled.

However, the carrier smoothing measurements are valid as long as the phase measurements are stable and not affected by carrier cycle slips. Impairments on the signal carrier phase, such as phase scintillations, can cause cycle slips, errors of one full cycle made by the receiver tracking loop in estimating the phase of the signal. Cycle slips, although being irrelevant for code-based measurements and for the purpose of estimating the carrier Doppler frequency, lead to errors in phase-based and carrier smoothed measurements and consequently to a degraded positioning performance.

3. Measurement Campaign Setup and Installation

The following section reports a description of the location, the data collection and of the system used for recording GNSS data. The data sets of interest collected in the Arctic are listed hereafter and discussed in section 4.

3.1. Installation at Svalbard

The use of GNSS in the Arctic has recently gained importance, due to the growth of human activities such as oil drilling, shipping, and tourism. Much attention was also given to risks related to decreased accuracy and reliability of the navigation solution (Gao et al., 2012). Furthermore, high-latitude regions are generally characterized by a poor satellite geometry and high GDOP values, further reducing the positioning quality (Jensen & Sicard, 2010). As an example, Figure 3 reports the skyplot of GPS, Global NAvigation Satellite System (GLONASS), BeiDou, and Galileo satellites in at Svalbard Islands, about 78°10′N.

In addition, the coupling between solar wind, magnetosphere, and ionosphere makes the Arctic regions significantly exposed to the formation of ionospheric irregularities (Kintner et al., 2009). In fact, the intensification of particle precipitation along the field lines under open magnetosphere conditions, the fragmentation of the tongue of ionization within the polar cap and the steep electron density gradients forming in correspondence with the equatorward and poleward boundaries of the auroral oval are the principal mechanisms leading to enhanced probability of scintillation effects on L-band signals cap (Jin et al., 2015; Moen et al., 2013; Spogli et al., 2009).

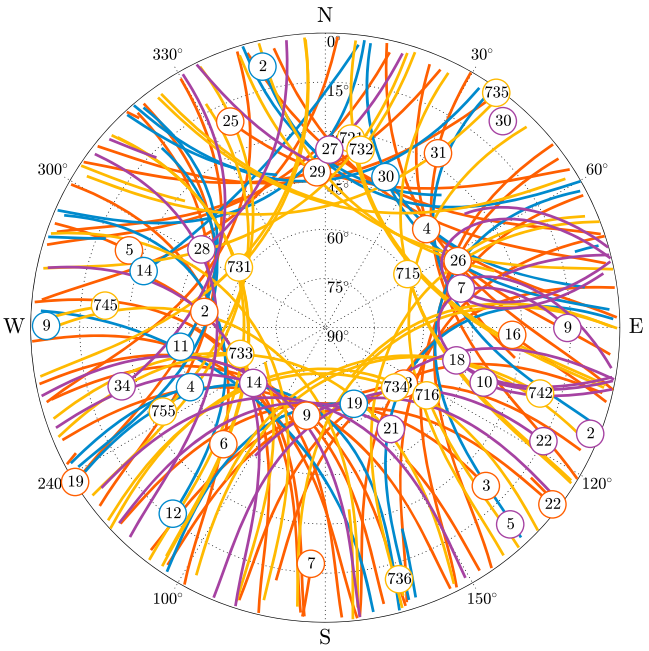


Figure 3. Visibility of Global Navigation Satellite System satellites over 24 hr: GPS (orange), GLONASS (yellow), Galileo (yellow), and Beidou (purple). Adventdalen, Svalbard Archipelago, 78°10′10.05″N.

The combination of low-elevation satellites and ionospheric scintillation makes navigation a critical task for such challenging environment. The monitoring of the quality of GNSS is indeed of great interest (Jensen & Sicard, 2010). Since 2004, a research station in Adventdalen, a remote valley nearby the city of Longyearbyen in Spitsbergen (main island of Svalbard archipelago, Norway), hosts a permanent GNSS monitoring station, shown in Figure 4. Geographic coordinates of the site are 78°10′10.05″N, 15°59′33.32″E; geomagnetic latitude is 74°91′N.

Customized GNSS receivers for ionospheric scintillation studies were installed in the frame of the project Ionospheric Scintillations Arctic Campaign Coordinated Observations, lead by the Italian Istituto Nazionale di Geofisica e Vulcanologia (De Franceschi et al., 2006). In addition, in September 2017, we carried out a GNSS data collection, by means of an SDR receiver.

3.2. SDR GNSS Receiver

An SDR GNSS data grabber and receiver, similar to the one described by Cristodaro et al. (2018), was installed in Adventdalen and was exploited for this work. Raw baseband samples of the GNSS signal were captured and digitalized through of a Universal Software Radio Peripheral (USRP) device and then postprocessed by means of a fully software non-real-time GNSS receiver, developed by the NavSAS group at Politecnico di Torino. GPS signals in the L1 band (1575.42 MHz) were captured and stored, as digital raw samples at $5 \cdot 10^6$ samples per second and at 8 bit per sample resolution, suitable for later postprocessing and analysis (Cristodaro et al., 2018). Working with self-made data grabbers and receivers granted the complete access to each stage of the system architecture and enabled higher levels of flexibility and reconfigurability. In addition, the availability of stored raw baseband samples of the signal allowed postprocessing of the original scenario, exploiting different architectures and configuration of the software receiver (Lachapelle & Broumandan, 2016).

SDR-based receivers are valuable alternative to ISMRs, as proven by Curran et al. (2014) and Peng and Morton (2013). Furthermore, it has been proven by Linty et al. (2016) that they provide scintillation indexes with the



Figure 4. Sousy Radar Station in Adventdalen Valley 78°10′10.05″N, 15°59′33.32″E, Longyearbyen, Spitsbergen (Norway).

Table 1
Summary of Significant Data Sets Captured by the SDR System in Svalbard During the September 2017 Storm

Date	Start time (UTC)	GPS PRNs affected	Maximum σ_Φ (rad)
07/09	22:59	13, 20, 28, and 30	0.5
08/09	06:08	6, 23, 25, 29, and 31	0.4
08/09	07:57	9 and 16	0.4
08/09	09:45	7	0.5
08/09	18:32	6, 9, and 23	1.2

Note. Date is formatted as DD/MM. SDR = software-defined radio; PRN = pseudorandom noise.

same quality of a professional commercial ISMR. As an example, this paper shows results of carrier smoothing positioning algorithm, which can be implemented and easily configured when using software GNSS receivers.

3.3. Summary of Data Collected

Ionospheric monitoring stations based on SDR systems are required to autonomously detect noticeable scintillation events and to automatically store raw GNSS signal samples. The SDR front-end was scheduled to continuously capture chunks of 30 min of data. The storage of the samples was triggered by a detection rule, defined as a threshold on the value of the scintillation indexes.

Between 3 and 15 September, the system automatically grabbed, processed, and stored 29 chunks of data, affected by moderate and strong scintillation, corresponding to 486 GB of data. All the captured data set were processed in NavSAS laboratory to identify true scintillation events. The most interesting captures have been selected and are reported in Table 1, along with the pseudo-random-noise code of the impaired signals.

4. Results

The geomagnetic storm-induced diffuse ionospheric scintillations on GNSS signals on 7–9 September 2017. This section reports the results related to four different data sets, selected among the list of data reported in Table 1:

1. 7 September 22:59 - moderate scintillation at the end of the grabbing interval;
2. 8 September 07:57 - low scintillation at the end of the grabbing interval;
3. 8 September 18:32 - strong scintillation at the beginning of the grabbing interval;
4. 5 September 16:24 - no scintillation, used as a benchmark.

First, linear trend of phase scintillations is shown, to identify the relevant events. Afterward, the smoothed position errors are analyzed. Higher errors are expected to be observed in the presence of scintillation. Position solution is then inspected toward the identification and discussion of a clustering phenomenon related to the occurrence of scintillations.

4.1. Phase Scintillation Index

The phase scintillation index as computed by the software GNSS receiver every minute for each visible satellite is reported in Figure 5 for the four data sets selected. The portions characterized by phase scintillation are outlined by an enclosing yellow box. It has to be mentioned that no relevant amplitude scintillation was detected. This is in agreement with the typical behavior of the polar ionosphere (Doherty et al., 2003).

The first panel reports the phase scintillation index related to the first case study, captured on 7 September at 22:59 UTC. While for the first part of the data set σ_ϕ never exceeds the noise floor (lower than 0.15 rad), moderate phase scintillation is detected on four satellites at the end of the grabbing interval.

Similarly, the phase scintillation index for the second case study is shown in the second panel of Figure 5. In this case, values of σ_ϕ slightly larger than 0.25 rad are detected at the end of the data collection for a single satellite.

The third panel reports the phase scintillation index for the third case study. Strong phase scintillation is detected on two signals at the beginning of the data set, until 18:43.

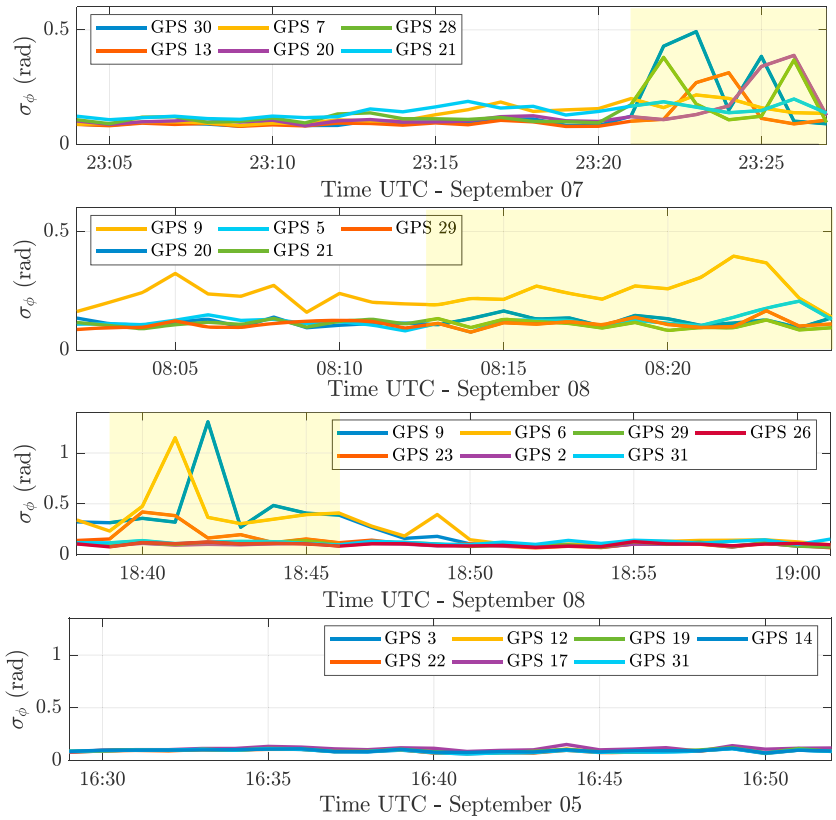


Figure 5. Phase scintillation index computed by the software receiver on the four different case studies analyzed. Yellow areas identify potential scintillation phenomena.

A fourth case study is selected, to compare results in the absence of scintillation. It corresponds to a chunk of data captured on 5 September, under quiet ionospheric conditions. No phase scintillation is detected, as σ_ϕ is always below 0.1 rad (bottom plot).

4.2. Analysis of the Positioning Error

The variation of visible satellites is not fast enough to justify a sudden degradation of the positioning solutions due to GDOP. Therefore, the positioning error is inspected hereafter to exclude other source of uncertainty thus supporting the influence of the scintillation events in the clustering.

The error of the estimated position solution $\hat{\mathbf{x}}(t)$, compared to the true solution $\mathbf{x}(t)$, is denoted $\epsilon(t)$. It is equal to the Euclidean distance between the two coordinates vectors:

$$\epsilon(t) = \sqrt{\left[\hat{x}(t) - x(t)\right]^2 + \left[\hat{y}(t) - y(t)\right]^2 + \left[\hat{z}(t) - z(t)\right]^2} \,. \tag{7}$$

For the sake of completeness, it could be useful to also consider the error standard deviation σ_ϵ. The standard deviation is computed on overlapping windows of the signal, of length equal to 30 s. In order to remove the contribution of the satellite geometry, the value of the standard deviation is then divided by the GDOP, according to (5).

A linear fit has been computed on both curves, to outline the trend of the error. The linear model is based on the fitting function $f(t)$, defined as

$$f(t) = a\sin(t - \pi) + b(t - 10)^2 + c \,, \tag{8}$$

where the coefficients a, b, and c are computed with 95% confidence bounds.

Figure 6 shows the error $\epsilon(t)$ and its standard deviation for the first data set, characterized by scintillation at the end of the capture. As reported in the upper panel of Figure 5, σ_ϕ increases above the scintillation threshold after 23:21 UTC. At the same time, the error on the position doubles. The linear fit clearly shows how the overall

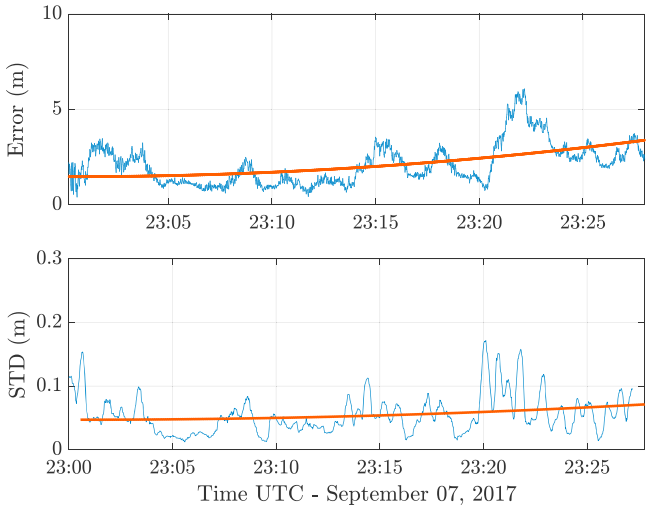


Figure 6. Positioning results in the presence of phase scintillation at the end of the capture. Error (top panel) and error Standard Deviation (STD) (bottom panel) with respect to the true position. The red curve is the linear fit.

trend of the positioning error matches the trend of the phase scintillation index. As a further confirmation of the fact that the worsening of the position solution is due to scintillation, the GDOP-free standard deviation is shown in the bottom panel of Figures 6–8. The same increasing trend can be noticed, with a slight increase of the error standard deviation due to phase scintillations.

Similar considerations can be drawn for the second case study analyzed, containing scintillation at the beginning of the capture. Figure 7 reports the positioning error, its standard deviation compensated by the GDOP, and their linear fits. Strong phase scintillations are present up to 18:42 UTC, as reported in Figure 5, and correspond to positioning errors up to 10 m. As long as scintillation decreases below 0.5 rad, the positioning error decreases. The linear fits confirm the trend.

To give a further confirmation that the highest error contribution is due to scintillation, a scintillation-free data set is considered. The results are depicted in Figure 8. No relevant scintillation activity was detected at the time. The error on the position is around 2 m and fairly constant over all the data set duration, as shown by the linear fit.

Any relevant increments in the GDOP-free standard deviation are observed in the experimental data. Positioning solutions are characterized by sudden biases, which are likely to be caused by ionospheric events.

4.3. Toward Detection of Scintillation Events Through Clustering of Positioning Solution

Results of the previous section showed how, in the presence of scintillation, positioning errors are affected by an increasing bias. In order to perform an automatic clustering of the realizations of $\hat{\mathbf{x}}$, k-means algorithm has been used. A binary clustering ($k = 2$) is suitable, in this case, to identify the boolean occurrence of a scintillation event by means of its effect on the positioning error. The algorithm establishes the occurrence of the event by considering only the positioning output without any need of additional training sets. This approach is usually known as unsupervised learning.

The k-means clustering algorithm is a widespread computationally efficient method to partition the observations of a multivariate random variable into k clusters (Lloyd, 1982). It employs a two-phase iterative algorithm to minimize the sum of point-to-centroid distances, summed over all k clusters. The algorithm first computes the centroids of the clusters and then iteratively establishes which observation belongs to them (Arthur & Vassilvitskii, 2007). For more details on centroids computation and implementation of k-means clustering algorithm, the readers are referred to Hartigan and Wong (1979). The k-means always looks for two clusters, but in absence of relevant phenomena, the separation of the computed centroids is expected to be small. The realizations of the positioning solution, $\hat{\mathbf{x}}$, are mapped to one of the two clusters according to the following rule:

- $\mathbf{x}(t)$ belongs to cluster 1, $i(t) = 1$;
- $\mathbf{x}(t)$ belongs to cluster 2, $i(t) = -1$.

Depending on the initial clustering, the indexes can be inverted but the transitions between the two choices are preserved, thus representing the target of this study.

By observing the positioning solution in an E-N-U coordinate system, the bias in the positioning error is particularly evident. As an example, Figure 9 shows the positioning results for three data sets (7 September 22:59, 8 September 07:57, and 8 September 18:32). The results have been plotted with a different color depending on the absence and presence of phase scintillation, according to the decision of the k-means algorithm. It is noticeable that the clusters are well separated for all the data sets affected by scintillation. On the contrary, when no scintillation is present, as in the

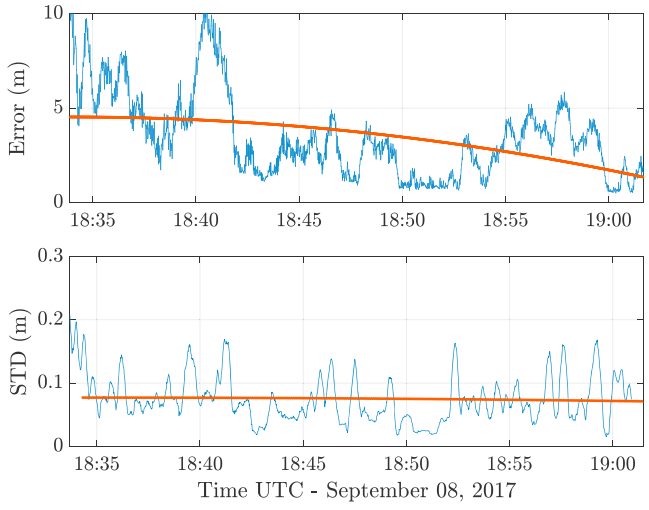


Figure 7. Positioning results in the presence of phase scintillation at the beginning of the capture. Error (top panel) and error Standard Deviation (STD) (bottom panel) with respect to the true position. The red curve is the linear fit.

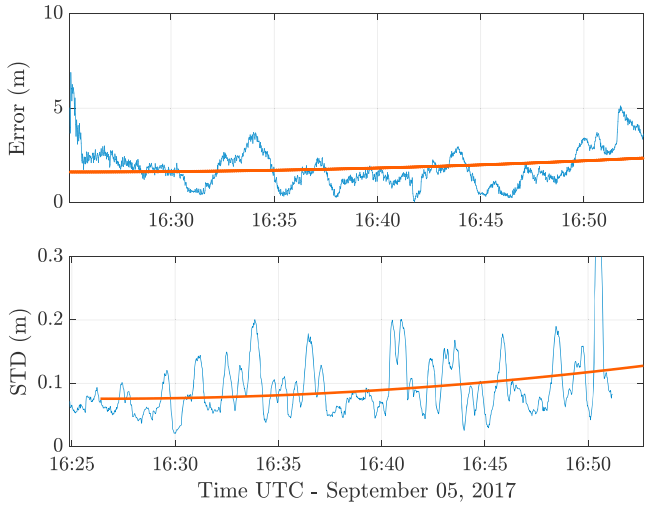


Figure 8. Positioning results in the absence of phase scintillation. Error (top panel) and error Standard Deviation (STD) (bottom panel) with respect to the true position. The red curve is the linear fit.

data set of 5 September, there is no evident separation between the two clusters. This is shown in the bottom right panel of Figure 9.

Although the variance of the two clusters does not provide significant information about the event, the bias is clearly visible in the case of points affected by scintillation. This outcome suggests then a novel way to detect scintillation, based on the effects on the positioning rather than on the observation of the signal quality or of each single measurement.

Figure 10 depicts the analysis of the time series of the clustering decision, $i(t)$. This off-line inspection allowed the determination of the instant in which a significant variation in the spatial distribution of points starts being observed. Such an instant is hereafter referred to t^* and is expected to match a transition between presence and absence of scintillation events.

In more details, Figure 10 depicts the superposition of the value of the scintillation indexes of all available satellites (blue), the positioning solution error (orange), the portion of data affected by scintillation according to a manual classification (yellow square), and the stepwise time series of the automatic clustering algorithm (black). It can be easily observed that there is a good correlation between the increment of the values of σ_ϕ and of the positioning error, in correspondence with t^*.

The clustering stepwise curve is able to correctly detect the scintillation events in all the data sets analyzed. It has to be noted that in the case of 8 September 18:32, although the scintillation event at the beginning is correctly identified, a false alarm is present after 18:54. A deeper investigation revealed that this is not caused by scintillation but likely by multipath. As outlined in section 3.1, due to the high-latitude location, after 18:50 many satellites exhibit very low elevation. The reduced number of satellites in view does not allow the

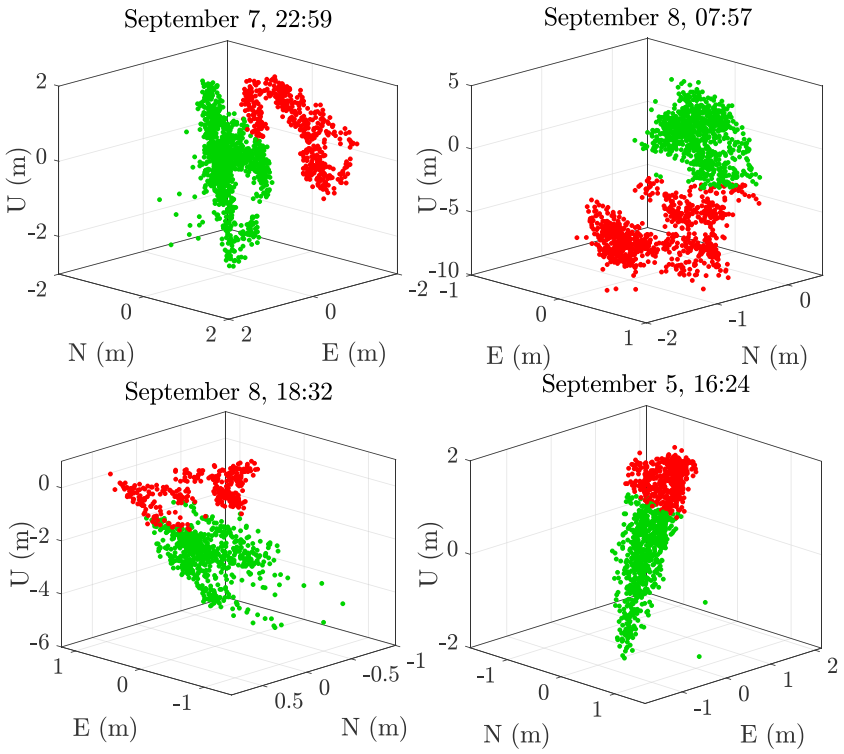


Figure 9. Positioning error of data sets affected by scintillation (7 September 22:59, 8 September 07:57, and 8 September 18:32) and not affected by scintillation (5 September 16:24).

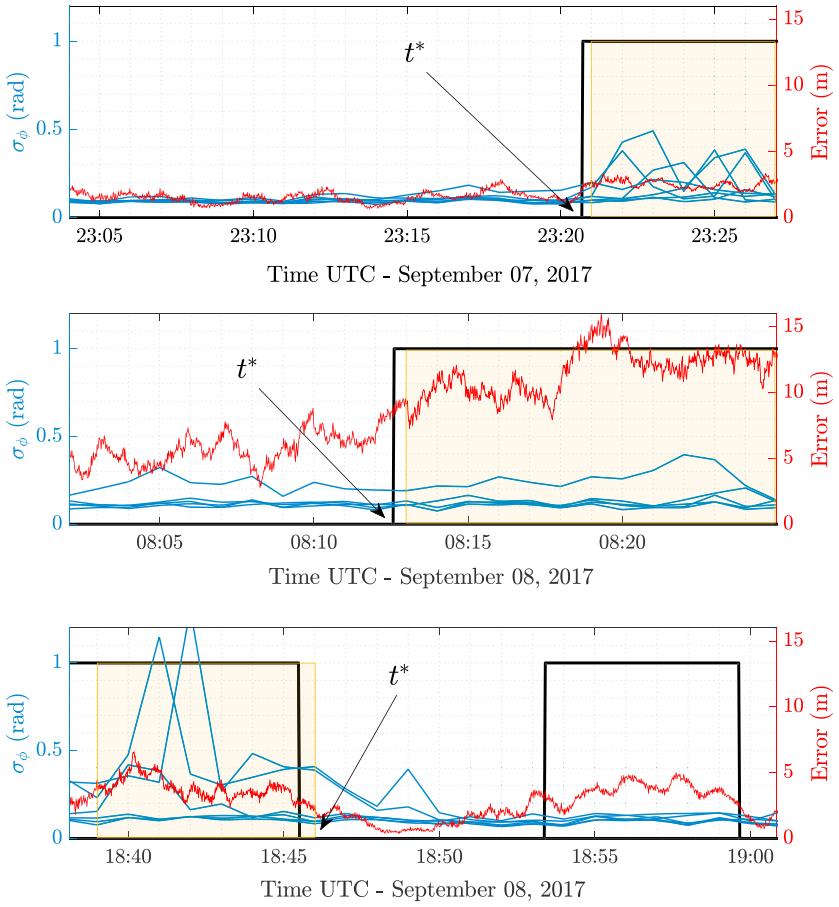


Figure 10. Comparison of σ_ϕ index for visible satellites (light blue), position solution error (orange), and clustering-derived detection (black).

exclusion of satellites below a certain elevation mask. As a consequence, large positioning errors are introduced, triggering a false scintillation detection.

4.4. Effect of the Smoothing Weight

As shown in Figure 10, the identified transition instants (black solid lines) are not perfectly aligned with the manually set reference (yellow area). This misalignment could be due to a random choice of the weight in the smoothing filters or to an inaccurate manual definition of the beginning of the phenomena. Formally, there is a dependency of the accuracy in the identification of the right transition instant, t^*, with respect to the smoothing weight W.

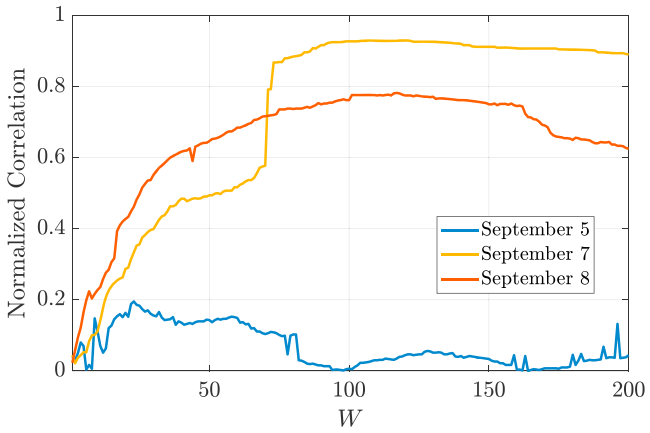


Figure 11. Correlation between clustering-defined and ground-truth times series, for different values of the smoothing weight W and for three different data sets (7 September 22:59, 8 September 18:32, and 5 September 16:24).

In order to determine an optimal value for parameter W, a search for the best match between the ground-truth and the automatic identification of t^* is performed. A ground-truth stepwise time series, $i^*(t)$, was defined according to the linear trend of σ_ϕ and used to validate the triggering accuracy of the clustering algorithm. The $i^*(t)$ was built according to the output frequency of the PVT solutions (i.e., 1 Hz), thus keeping the same number of available positions. The correctness of the time series derived from the clustering was evaluated by means of cross correlation (Kay, 2013):

$$R_W(k) = E[i^*(t-k) * i_W(t)] \,, \tag{9}$$

where E is the operand of the statistical average. The normalized peak values of the R_W were then collected, for different realizations of the clustering with $W \in [1, 200]$.

The results for three different data sets are reported in Figure 11. As expected, the scintillation-free data set exhibits a very low correlation with the ground-truth, always below 0.2. In the presence of scintillation, higher values of correlation between ground-truth and clustering time series are obtained. In particular, the maximum correlation is obtained for W between 110 and 120. This means that such weights of the smoothing filter determine a major separation in the clustering process, thus guaranteeing a better identification of the scintillation start and end time. On the other hand, the employment of such values for a precise positioning emphasizes dramatically the effect of the ionospheric event on the accuracy of the solution.

It is interesting to notice that the case $W = 1$ is equivalent to employ code-based only measurements. In this situation, it is impossible to recognize the scintillation event, as code noise dominates the positioning error. As long as the value of W increases, the carrier smoothed measurements are more and more relevant; the noise of the smoothed pseudorange is reduced and the contribution of error due to scintillation is more and more visible. For larger values of W, beyond 150–160, the solution obtained through carrier smoothing is no longer reliable. The main contribution of error becomes the code-carrier divergence.

5. Conclusions

Three different GPS data sets, recorded on early September 2017, at Longyearbyen, Svalbard, were analyzed in this study. Moderate and strong phase scintillation were detected on 7 and 8 September, as a consequence of the concurrent geomagnetic storm. The effect on the GPS positioning solution was evaluated, by means of a software receiver implementing the carrier smoothing algorithm. Significant increments of the bias of the positioning error were observed during scintillation events. Similarly, the error variance, properly corrected by the GDOP, showed a match with the intensity of phase scintillation. Furthermore, the horizontal position solutions showed a clear clustering effect, allowing to separate scintillated points from non-scintillated points. It was proven that clustering based on carrier smoothing position solutions is an effective method to determine the error transition induced by arising and fading of scintillation events. The efficiency of the method was verified for different weights of the carrier smoothing algorithm up to the identification of an optimal value, which emphasizes the effect of the scintillation.

The inspection of data sets with stronger scintillations in different geographical areas is expected to better assess the results of the current study. As further research, a better design of the clustering algorithm with an extended position vector is advisable as well as the capability of performing online clusterization each time positioning solutions are computed. Furthermore, the evaluation of a metric such as the separation of the clusters can provide a measure of integrity of GNSS positioning during next severe geomagnetic storms.

Acronyms

CME = Coronal Mass Ejection
ECEF = Earth Centered Earth Fixed
DST = Disturbance Storm Time
GDOP = Geometrical Dilution Of Precision
ISMR = Ionospheric Scintillation Monitoring Receiver
LMS = Least Mean Square
PVT = Position, Velocity and Time
GNSS = Global Navigation Satellite System
UERE = User Equivalent Range Error
SDR = Software-Defined Radio
SSC = Sudden Storm Commencement
USRP = Universal Software Radio Peripheral
GPS = Global Positioning System
GLONASS = GLObal NAvigation Satellite System

Acknowledgments
DST data shown in this study are provided by the World Data Center of Kyoto (http://wdc.kugi.kyoto-u.ac.jp/dstdir/). The true reference position has been obtained by processing 24 hr of RINEX files by means of the AUSPOS Online GPS Processing Service (version: AUSPOS 2.3). We are grateful to the people working for the ISACCO project (Ionospheric Scintillations Arctic Campaign Coordinated Observations) hosted by University of Tromsø within the infrastructure of the Sousy Svalbard Radar.

References

Alfonsi, L., Spogli, L., De Franceschi, G., Romano, V., Aquino, M., Dodson, A., & Mitchell, C. N. (2011). Bipolar climatology of GPS ionospheric scintillation at solar minimum. *Radio Science*, *46*, RS0D05. https://doi.org/10.1029/2010RS004571

Arthur, D., & Vassilvitskii, S. (2007). k-means++: The advantages of careful seeding. In *Proceedings of the eighteenth annual ACM-SIAM symposium on Discrete algorithms* (pp. 1027–1035).

Basu, S., Groves, K., Basu, S., & Sultan, P. (2002). Specification and forecasting of scintillations in communication/navigation links: Current status and future plans. *Journal of Atmospheric and Solar-Terrestrial Physics*, *64*(16), 1745–1754.

Bradford, P. W., Spilker, J., & Enge, P. (1996). *Global Positioning System: Theory and applications* (Vol. 109). Washington, DC: American Institute of Aeronautics and Astronautics.
Cristodaro, C., Dovis, F., Linty, N., & Romero, R. (2018). Design of a configurable monitoring station for scintillations by means of a GNSS software radio receiver. *IEEE Geoscience and Remote Sensing Letters*, *15*, 325–329.
Curran, J., Bavaro, M., Fortuny-Guasch, J., & Morrison, A. (2014). Developing an ionospheric scintillation monitoring receiver. Inside GNSS, September–October.
De Franceschi, G., Alfonsi, L., & Romano, V. (2006). ISACCO: An Italian project to monitor the high latitudes ionosphere by means of GPS receivers. *GPS Solutions*, *10*(4), 263–267.
De Franceschi, G., Alfonsi, L., Romano, V., Aquino, M., Dodson, A., Mitchell, C. N., et al. (2008). Dynamics of high-latitude patches and associated small-scale irregularities during the October and November 2003 storms. *Journal of Atmospheric and Solar-Terrestrial Physics*, *70*(6), 879–888.
Doherty, P. H., Delay, S. H., Valladares, C. E., & Klobuchar, J. A. (2003). Ionospheric scintillation effects on GPS in the equatorial and auroral regions. *Navigation*, *50*(4), 235–245.
Dubey, S., Wahi, R., & Gwal, A. (2006). Ionospheric effects on GPS positioning. *Advances in Space Research*, *38*(11), 2478–2484.
Forte, B. (2007). On the relationship between the geometrical control of scintillation indices and the data detrending problems observed at high latitudes. *Annals of Geophysics*, *50*(6), 699–706.
Gao, G. X., Heng, L., Walter, T., & Enge, P. (2012). Breaking the ice: Navigation in the Arctic. In *Global Navigation Satellite Systems: Report of a Joint Workshop of the National Academy of Engineering and the Chinese Academy of Engineering* (pp. 229–238). National Academies Press.
Groves, K., Basu, S., Quinn, J., Pedersen, T., Falinski, K., Brown, A., et al. (2000). A comparison of GPS performance in a scintillation environment at Ascension Island. In *Proceedings of the 13th International Technical Meeting of the Satellite Division of The Institute of Navigation (ION GPS 2000)* (pp. 672–679). Salt Lake City, UT. September 2000.
Hartigan, J. A., & Wong, M. A. (1979). Algorithm AS 136: A k-means clustering algorithm. *Journal of the Royal Statistical Society. Series C (Applied Statistics)*, *28*(1), 100–108.
Jensen, A. B., & Sicard, J.-P. (2010). Challenges for positioning and navigation in the Arctic. Coordinates: A resource on positioning, navigation, and beyond.
Jiao, Y., Morton, Y. T., Taylor, S., & Pelgrum, W. (2013). Characterization of high-latitude ionospheric scintillation of GPS signals. *Radio Science*, *48*, 698–708. https://doi.org/10.1002/2013RS005259
Jin, Y., Moen, J. I., & Miloch, W. J. (2015). On the collocation of the cusp aurora and the GPS phase scintillation: A statistical study. *Journal of Geophysical Research: Space Physics*, *120*, 9176–9191. https://doi.org/10.1002/2015JA021449
Kay, S. M. (2013). *Fundamentals of statistical signal processing: Practical algorithm development* (Vol. 3). Boston, MA: Pearson Education.
Kintner, P., Humphreys, T., & Hinks, J. (2009). GNSS and ionospheric scintillation: How to survive the next solar maximum, Inside GNSS. july/august 2009.
Lachapelle, G., & Broumandan, A. (2016). Benefits of GNSS IF data recording. In *Proceedings of the 2016 European Navigation Conference (ENC)* (pp. 1–6). IEEE.
Linty, N., Romero, R., Cristodaro, C., Dovis, F., Bavaro, M., Curran, J. T., et al. (2016). Ionospheric scintillation threats to GNSS in polar regions: The DemoGRAPE case study in Antarctica. In *European Navigation Conference (ENC 2016)* (pp. 1–7). IEEE.
Linty, N., Romero, R., Dovis, F., & Alfonsi, L. (2015). Benefits of GNSS software receivers for ionospheric monitoring at high latitudes. In *1st URSI Atlantic Radio Science Conference (URSI AT-RASC 2015)* (pp. 1–6). IEEE.
Lloyd, S. (1982). Least squares quantization in PCM. *IEEE transactions on Information Theory*, *28*(2), 129–137.
Misra, P., & Enge, P. (2006). *Global Positioning System: Signals, measurements and performance* (2nd ed.). Lincoln, MA: Ganga-Jamuna Press.
Moen, J., Oksavik, K., Alfonsi, L., Daabakk, Y., Romano, V., & Spogli, L. (2013). Space weather challenges of the polar cap ionosphere. *Journal of Space Weather and Space Climate*, *3*, A02.
Myer, G. T., & Morton, Y. T. J. (2018). Ionosphere scintillation effects on GPS measurements, a new carrier-smoothing technique, and positioning algorithms to improve accuracy. In *Proceedings of the 2018 International Technical Meeting of The Institute of Navigation* (pp. 420–439). Reston, VA.
Peng, S., & Morton, Y. (2013). A USRP2-based reconfigurable multi-constellation multi-frequency GNSS software receiver front end. *GPS Solutions*, *17*(1), 89–102.
Petovello, M., Lo Presti, L. M., & Visintin, M. (2015). Can you list all the properties of the carrier-smoothing filter? *INSIDE GNSS*, *10*(4), 32–37.
Schwadron, N., Rahmanifard, F., Wilson, J., Jordan, A., Spence, H., Joyce, C., et al. (2018). Update on the worsening particle radiation environment observed by crater and implications for future human deep-space exploration. *Space Weather*, *16*, 289–303. https://doi.org/10.1002/2017SW001803
Spogli, L., Alfonsi, L., Cilliers, P. J., Correia, E., De Franceschi, G., Mitchell, C. N., et al. (2013). GPS scintillations and total electron content climatology in the southern low, middle and high latitude regions. *Annals of Geophysics*, *56*(2), 0220.
Spogli, L., Alfonsi, L., De Franceschi, G., Romano, V., Aquino, M., Dodson, A., et al. (2009). Climatology of GPS ionospheric scintillations over high and mid-latitude European regions. In *Annales Geophysicae*, EGU.
Tassev, Y., Velinov, P. I., Tomova, D., & Mateev, L. (2017). Analysis of extreme solar activity in early September 2017: G4 — Severe geomagnetic storm (07–08.09) and GLE72 (10.09) in solar minimum. *Comptes rendus de l'Acade'mie bulgare des Sciences*, *70*(10), 1437–1444.
Van-Dierendonck, A. J., Klobuchar, J., & Hua, Q. (1993). Ionospheric scintillation monitoring using commercial single frequency C/A code receivers. In *Proceedings of the 6th International Technical Meeting of the Satellite Division of The Institute of Navigation (ION GPS 1993)* (pp. 1333–1342).
Vanlommel, P., & Van der Linden, R. (2017). STCE newsletter 4 Sep 2017 – 10 Sep 2017.
Wernik, A. W., Alfonsi, L., & Materassi, M. (2004). Ionospheric irregularities, scintillation and its effect on systems. *Acta geophysica polonica*, *52*(2), 237–249.